

Beam Induced Fluorescence (BIF) Monitor for Intense Heavy Ion Beams *

F. Becker^{1†}, C. Andre¹, F. M. Bieniosek³, P. Forck¹, P. A. Ni³, D.H.H. Hoffmann²

¹GSI, Darmstadt, Germany; ²TUD, Darmstadt, Germany; ³LBNL, Berkeley, USA

Abstract

Non-intercepting **Beam Induced Fluorescence (BIF)** monitors measure transversal beam profiles by observation of fluorescence light originating from excited residual gas molecules. Thus they are an alternative to conventional intercepting devices. Single photon counting is performed using an image intensified digital CCD camera. We investigated the BIF process in the energy range of 7.7 keV/u to 750 MeV/u in residual nitrogen. Experiments at low beam energies were performed at a Marx-accelerator (NDCX) at Berkeley Lab [1] whereas mid and high energy experiments were carried out at GSI accelerators [2, 3]. Especially in the vicinity of targets the neutron-generated radiation level limits the monitor's signal to background ratio. Therefore the radiation background was investigated for different ion species and particle energies. Background simulations using a Monte Carlo transport code are compared to experimental data taken with scintillators, thermo luminescence detectors and the BIF monitor. Alternative image intensifier techniques are presented as well as shielding concepts. Furthermore the dynamics of ionized nitrogen molecules in the electric field of intense ion beams is discussed.

THE BIF METHOD AND APPLICATION

When beam ions collide with residual gas molecules, some molecules are ionized remaining in an excited state with a certain probability. In a N_2 -dominated residual gas composition, a strong fluorescence at $390 \text{ nm} < \lambda < 470 \text{ nm}$ (blue), of about 60 ns lifetime, is generated by a transition band to the N_2^+ electronic ground state ($B^2\Sigma_u^+(v') \rightarrow X^2\Sigma_g^+(v'') + \gamma$, for vibrational levels v) [4]. 'Single-photon counting' was performed with a commercial image intensifier [5], equipped with a double Micro-Channel Plate (MCP) for up to 10^6 -fold photo-electron amplification. Green light from a P46 phosphor screen of 300 ns decay time is taper-coupled to a digital CCD camera with a IEEE-1394a interface [6]. The device is mounted on a fused silica viewport at a distance of 20 cm from the beam axis. Remote controlled CCTV lenses with focal distances of 8 to 25 mm, lead to typical resolutions of 100-500 $\mu\text{m}/\text{pixel}$. Beam profiles were recorded on a single shot basis. To select specific transitions, 10 nm narrow band interference filters were installed in the optical path. A more detailed description of the experimental setup can be found in [7, 8, 9, 11].

* Work supported by EU, project FP6-CARE-HIPPI

† Frank.Becker@gsi.de

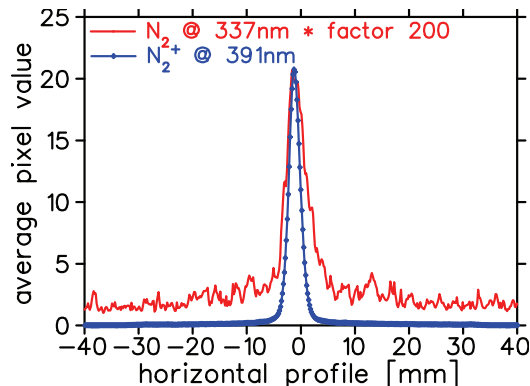


Figure 1: Beam profiles of a $10 \mu\text{A}$ 5.4 MeV/u Ni^{6+} beam in 10^{-3} mbar nitrogen, recorded with spectral filters [9]. The N_2^+ profile @ 391nm shows a σ of 1.1mm whereas N_2 profile @ 337nm has a σ of 2mm.

This paper will focus on issues related to the challenging beam parameters of the FAIR-facility [3] like energies well above 100 MeV/u in considerable loss induced radiation environments and E-field induced profile falsifications for intense and strongly focused beams. During the last years the BIF method was applied successfully at the GSI heavy ion LINAC for various ion species and energies between 5 and 11.4 MeV/u [7, 8, 9]. An additional setup was installed behind the heavy ion synchrotron SIS-18 in a high energy beam transfer line (HEBT) close to a dump. Due to the beam energy between 60 and 750 MeV/u this location allowed to determine the radiation impact on the detector performance. In addition this part of the beam pipe was separated by vacuum windows so that residual gas densities from base-pressure 10^{-8} mbar up to atmospheric pressure could be applied. Systematic investigation of profile falsifications have shown that beam profile width remains constant up to nitrogen pressures of about 1 mbar and also, that N_2 transitions lead to increased profile width $\geq 40\%$ compared to ionic N_2^+ transitions [9], see Fig.1. Cross sections for heavy ion induced transitions in N_2^+ are predominant compared to electron induced transitions. Unlike transitions in neutral working gases (N_2) which show enlarged beam profiles due to the secondary electron halo [10]. Although the contribution of N_2 transitions is $\leq 20\%$ and in the near UV, it should be suppressed by optical filters and discriminated against the desirable N_2^+ transitions at (391, 428, 470nm) [9]. For typical beam parameters at GSI LINAC and high energy beam transfer lines, profiles recorded with the BIF-monitor complied with SEM-grid (Secondary Electron Monitor) measurements within 10% [11], see Fig.2.

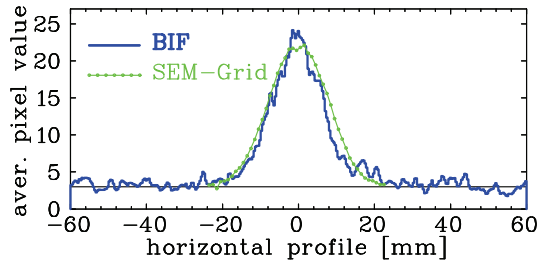


Figure 2: Beam profiles recorded with the BIF-Monitor and a SEM-Grid agree within 10%. $1.5 \mu\text{s}$ pulse of $2 \cdot 10^9$ Xe^{48+} at 200 MeV/u in HEBT line [11].

RADIATION IMPACT ON THE MONITOR

In the vicinity of production targets like the \bar{p} -target, the Super Fragment Separator-target (SFRS), or solid targets for plasmaphysics, a considerable amount of beam ions generates radiation which cannot be avoided. Our experimental area in a SIS-18 HEBT line is located just 2.1 m from the beam dump (Fe). Since all beam particles are stopped in the dump, the generated dose is comparable to fixed target experiments [12, 13]. Therefore radiation impact on the BIF-monitor was investigated in a realistic environment. During the first campaign a specific scaling of signal amplitude and background level with the beam energy was recognized [11]. Recent measurements for slowly extracted uranium ions of complementary energies are in good agreement with the 2005 data, although an Intensified CCD-camera (ICCD) with a different response characteristic and reproduction scale had to be used, see Fig.3. However, the signal amplitude scales with the Bethe Bloch law, whereas the background level scales with $\propto E^2$. With Li^6 Li^7 thermoluminescence dosimeters $\geq 83\%$ of the total dose was determined as neutrons [14]. A semi-empirical neutron production yield for heavy ion projectiles ≥ 5 MeV/u in thick heavy metal targets estimates neutrons per incident projectile, where N_T is the neutron number of the target and E_P is the incident projectile energy in MeV/u, see Eq.1 [13].

$$Y = \frac{1.5 \cdot 10^{-6}}{N_T^{1/3}} E_P^2 (A_P^{1/3} + A_T^{1/3})^2 N_P \frac{A_P}{Z_P^2} \quad (1)$$

This neutron yield scales with E^2 , like the background level recorded with the BIF-monitor. Therefore the neutron flux in our experimental cave as well as the neutron energy- and TOF spectra were simulated with the Monte Carlo transport code PHITS for a 200 MeV/u Xe^{48+} beam [12]. With fast plastic-scintillator-based, neutron sensitive detectors we recorded decaying background levels which complied with the simulated TOF-spectra [11]. The total simulated neutron flux per incident projectile and area integrated over all neutron energies is equally distributed and amounts between 10^{-3} and 10^{-6} , which is more than 1000 neutrons on the 5cm^2 photo cathode for 10^9 , 200 MeV Xe-ions per pulse. The simulated neutron energy spectrum (see Fig.4) predicts energies $E_n \geq 1$ MeV for $\leq 20\%$ of the

Transverse profile measurements and diagnostics systems

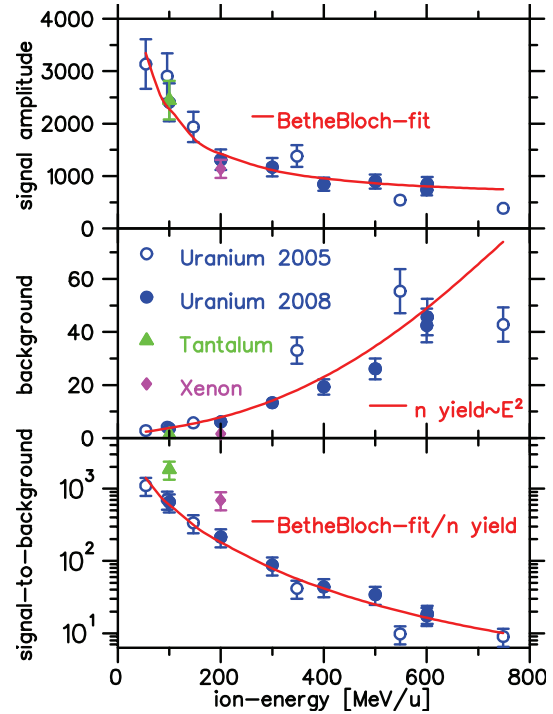


Figure 3: The total signal amplitude (top), background level (middle) and signal-to-background ratio (bottom) as a function of energy for the investigated ions. The signal amplitudes for Xe and Ta were normalized by their charge and mass with respect to U. The background was normalized with respect to the mass only.

generated neutrons. Since the thermal neutron peak at $\sim 4 \cdot 10^{-8}$ MeV [15] was cut off in that simulation, the low-energy part of the spectrum is even more predominant. As charged particles have even shorter ranges in matter (dump, beam-pipe, camera housing), shorter lifetimes $\leq \text{ms}$, or both - the essential contribution to the total radiation dose at the detector is neutrons and neutron-induced gammas. The signal to background ratio decreases by two orders of magnitude for E_P from 60 to 600 MeV/u. One order is due to increasing background level in this energy range. Thus the radiation impact on the intensified camera system has to be reduced.

ICCD VS. EMCCD CAMERA

One way to reduce the background contribution concerns the camera sensor and the radiation total cross section for alternative sensor materials. Our ICCD camera is equipped with a S-20 multi-alkali (Na_2KSb)Cs photocathode which was identified to cause the background signal [11]. Another competing technique is the silicon-based Electron Multiplying EM-CCD camera which has an additional gain register, based on avalanche diodes between the shift register and output amplifier, for single-photon detection applications [16]. The specific EMCCD sensor [17] we used was thinned to $15 \mu\text{m}$, back illuminated and Peltier-cooled down to -80°C . Neutron and photon total cross sections

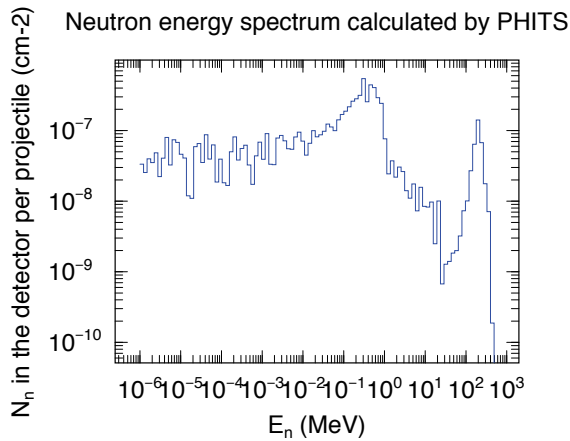


Figure 4: Energy spectrum as counting rate per incident projectile in log energy bins, at the BIF-monitor position, 2,1m from the dump - for a 200 MeV/u Xe beam [12].

from accessible databases [18] have been weighted stoichiometrically for S-20 and silicon, see Fig.5. S-20 shows a ~ 1 order of magnitude higher radiation total cross section for neutrons and gammas over the whole energy range, except for energies with nuclear resonances from 10^{-1} to 10 MeV. If the cross section is normalized to the detector surface and mass densities following Eq.2 (EMCCD/ICCD), the silicon data (blue) has to be multiplied by a factor of 2.37 to obtain the relative camera sensitivity. Nevertheless this estimation still predicts a lower radiation sensitivity for the EMCCD camera.

$$\frac{A_{em} \cdot d_{em} \cdot m_{A,em}}{A_{iccd} \cdot d_{iccd} \cdot \tilde{m}_{A,iccd}} = \frac{0.66 \text{cm}^2 \cdot 15 \mu\text{m} \cdot 28}{4.91 \text{cm}^2 \cdot 0.5 \mu\text{m} \cdot 46} = 2.37 \quad (2)$$

In order to check this prediction, we set up an experiment to compare both camera systems [5, 19] with identical source to sensor distances (c-mount $\hat{=}$ 17,52 mm + 4 mm for Pb-shielding), see Fig.6. As radiation sources, we used ^{60}Co (76 MBq) and ^{241}Am (3.52 MBq) as γ -emitters and a ^{241}Am -Be hybrid source as neutron emitter ($2.1 \cdot 10^4 \text{n}/(\text{s} \cdot 4\pi)$). All γ energies are listed in [18] and neutron energy spectra have been measured with a TOF-energy spectrometer as E_n between 1 and 10 MeV with peaks at 3 and 5 MeV [20]. For the Am-Be source we had to discriminate the neutron radiation against the ^{241}Am γ radiation with a 4 mm Pb shielding between source and camera system. This way there was just ~ 1 primary γ left per 100 neutrons at the detector surface. In this experiment we averaged over 100 images of 1 s integration time. Radiation background levels are listed in Tab.1. The EMCCD camera showed a 12-times higher dark noise level but in the radiation tests, the ICCD camera was between 2.0 and 3.4-times more sensitive for γ radiation and still 1.5-times more for neutrons and neutron induced γ radiation, which a priori cannot be distinguished from each other.

Second part of this comparison was the camera performance working as a BIF-monitor in single photon detection mode. For that purpose we installed both systems one af-

Transverse profile measurements and diagnostics systems

Table 1: Relative radiation background levels normalized to the 8 and 16-bit dynamics, dark noise subtracted.

Source	E[keV]	ICCD	EM	I/EM
darknoise	-	9.4E^{-5}	1.1E^{-3}	8.5E^{-2}
$^{241}\text{Am}/\gamma$	13.9;59.5	8.8E^{-2}	2.6E^{-2}	3.4
$^{60}\text{Co}/\gamma/\text{Pb}$	1173;1332	4.3E^{-1}	2.1E^{-1}	2.0
Am-Be/n	10^3 - 10^4	1.9E^{-3}	1.3E^{-3}	1.5

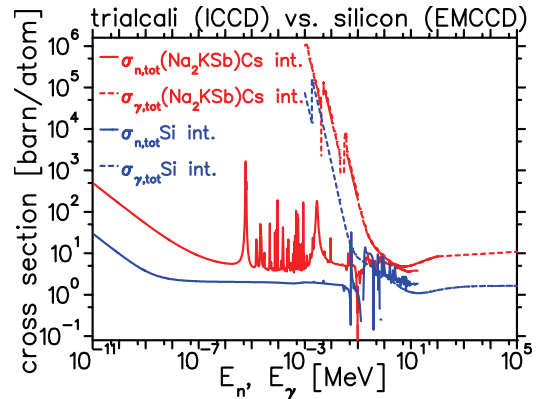


Figure 5: Total neutron and gamma cross sections for S-20 (weighted, red) and silicon (blue) from databases [18].

ter another at the GSI LINAC beamline with reproducible beam parameters (1.2 ms, $60 \mu\text{A}$, Ni^{13+}), N_2 pressures and the same lens ($f=16$ mm, $f/1.4$). Exemplary for five different pressures, relative signal amplitudes are shown in Tab.2. For pressures $\geq 5 \cdot 10^{-6}$ mbar the ICCD camera showed a 30-times higher signal amplitude, for pressures below it was even better, due to its negligible dark noise level Tab.1. This aspect can be understood with respect to Fig.7 and Fig.8, where BIF images and corresponding projections are plotted. However, the EMCCD camera had a 5-times higher resolution, because of constantly small single photon spots, even at highest gain levels compared to the ICCD which showed increasing spots sizes for increasing gain levels.

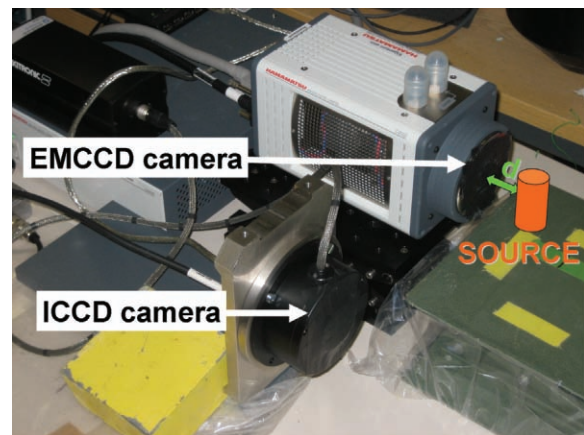


Figure 6: Photograph of the experimental setup. Radiation tests with Am, Co γ sources and a Am-Be neutron source in front of EMCCD and ICCD camera.

Table 2: Relative signal amplitude normalized to the 8 and 16-bit dynamics, dark noise subtracted.

p_{N_2} [mbar]	ICCD	+FB	EM	I/EM
$1 \cdot 10^{-6}$	$5.5E^{-3}$	-	$7.6E^{-5}$	72
$5 \cdot 10^{-6}$	$3.2E^{-2}$	-	$1.1E^{-3}$	29
$1 \cdot 10^{-5}$	$6.8E^{-2}$	-	$2.6E^{-3}$	26
$5 \cdot 10^{-5}$	$2.9E^{-1}$	$7.1E^{-3}$	$9.7E^{-3}$	30
$1 \cdot 10^{-3}$	-	$1.8E^{-1}$	$2.3E^{-1}$	-

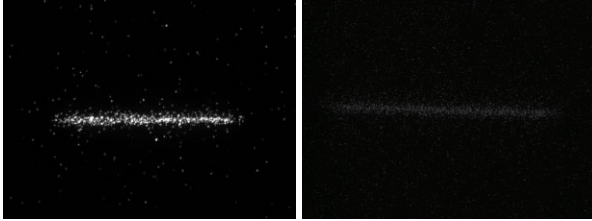


Figure 7: BIF-images of an 1.2 ms, 60 μA , Ni^{13+} beam in 10^{-4} mbar N_2 , recorded with a ICCD (left) and a cooled EMCCD (right) [19].

FIBEROPTIC IMAGE BUNDLE

Another way to approach the radiation issue is to enclose the detector system in an appropriate shielding. A multi-shell concept for moderation and capture of MeV neutrons and absorption of neutron induced γ radiation requires a shielding thickness of ~ 1 m [21]. Since the imaging is sensitive to the solid angle Ω by $1/r^2$, it has to be conserved. This can be realized by a telescope setup or a fiberoptic image bundle, which maintains mechanical flexibility, see Fig.9. In order to preserve the optical resolution of the whole imaging system, the fiber size, packing density and active surface were adapted to parameters of the MCP (10 μm , 60 lp/mm, 12x12mm). Only for practical reasons the fiber bundle was coupled to the ICCD with a 1:1 relay optics. The actual losses in the relay optics, compared to direct coupling will be measured shortly, but a conservative estimate for the acceptance is $NA \sim [n \cdot \sin(\arctan(1/(2\kappa)))]^2 = 3.1\%$ with $f = 2.8$. The 1.2m image bundle is specified to have a

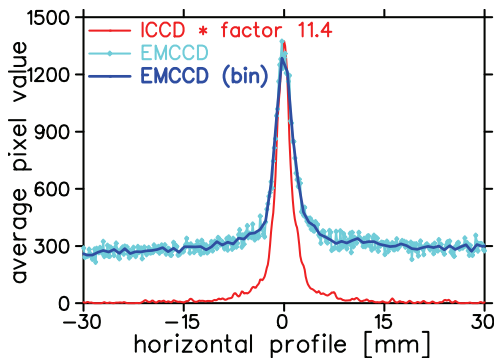


Figure 8: Projected beam profiles of a 60 μA , Ni^{13+} beam in 10^{-4} mbar N_2 , recorded with ICCD (8-bit) and EMCCD (16-bit) camera. To compensate the 5-times higher resolution of the EMCCD, profile was binned by a factor 5.

Transverse profile measurements and diagnostics systems

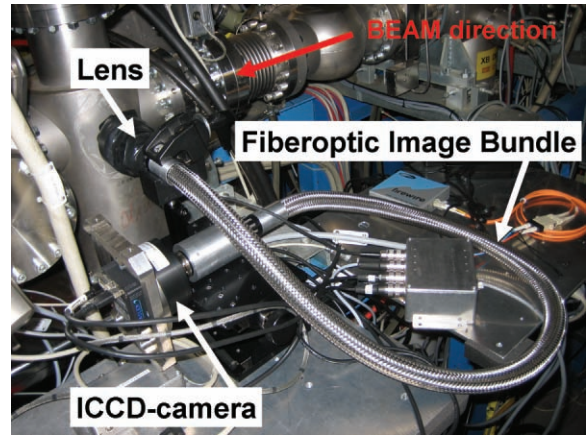


Figure 9: The 1.2 m fiberoptic image bundle mounted at the UNILAC test setup. In a later shielding assembly, the fiber bundle will not be furled.

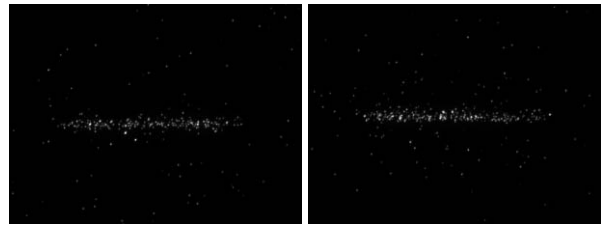


Figure 10: BIF-images of an 1.2 ms, 60 μA , Ni^{13+} beam, recorded with a ICCD in $2.5 \cdot 10^{-5}$ mbar N_2 (left) and with the ICCD mounted on the 1.2 m fiberoptic image bundle in 10^{-3} mbar N_2 (right), see Figure 9.

spectral transmission of 35% at 400 nm. We measured the total performance of the ICCD coupled to an image bundle at BIF-setup at GSI UNILAC. As shown in Tab.2 (third column), relative signal amplitude decreases by a factor of 40 ($5 \cdot 10^{-5}$ mbar), compared to the ICCD without the image bundle. Whereas signal quality is maintained in this setup, see Fig.10 and in particular, see Fig.11.

HOW THE E-FIELD AFFECTS PROFILES

Singly charged N_2^+ ions are accelerated in the E-field of an ion bunch. Their trajectories from the position of ex-

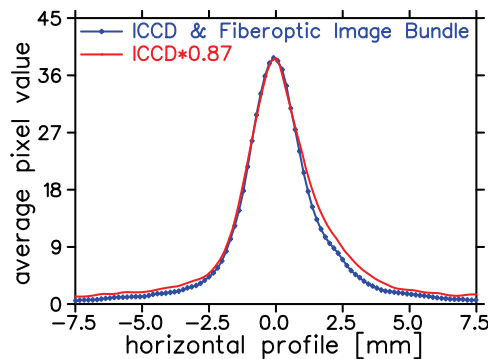


Figure 11: Experimental conditions of Fig.10. Comparison of profiles with the fiber bundle (blue) and without (red). Averaged over 100 images to improve statistics.

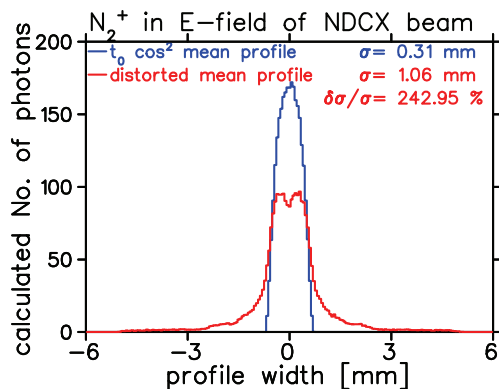


Figure 12: Monte Carlo simulation of projected N_2^+ trajectories in the electric field of $5 \cdot 10^{11} K^+$ @ 7,69 keV/u in $3 \mu s$, focused down to 0.3 mm as in the NDCX target chamber [1].

citation to the crucial position of spontaneous decay and photo-emission after a specific lifetime can be calculated. Precise E-field modeling is the basis for a Monte Carlo simulation code [22]. As for \cos^2 charge distributions, Maxwell's equations can be solved analytically, this distribution was chosen to approximate the Gaussian charge distribution in ion bunches. Trajectories had to be weighted incrementally in time with the decay-frequency of excited states ($\tau=60ns$). Finally all simulated trajectories (~ 25000 points per data-set) are projected and plotted as counting rate, representing a beam profile. A $5 \cdot 10^{11} K^+$ beam @ 7,69 keV/u of $3 \mu s$ bunch length was simulated as the blue \cos^2 distribution, see Fig.12. For $E_{r,max}=65$ kV/m and $\tau_{N_2^+}$ a hollow shaped distribution (red) was obtained. GSI beam parameters are currently not as critical as those, but we are considering different working gases with shorter lifetimes.

CONCLUSION

The comparison between ICCD and EMCCD cameras as BIF-monitors showed an intrinsically lower radiation sensitivity for the EMCCD camera, namely a factor of 1.5 to 3.4, see Tab.1. Although the EMCCD's relative signal performance is a factor of 30 lower, it resolves beam profiles comparable to the ICCD-type, see Tab.2. This was achieved due to its higher resolution (factor 5) with applied binning and due to its higher dynamic range (16-bit for that specific model). For lowest light-intensity applications with few photons, another point for the EMCCD is the 4-times higher quantum efficiency (for thinned, back-illuminated sensors) leading to less shot noise and better statistics [17]. Since former experiments with a front-illuminated EMCCD, cooled to $-12^\circ C$ showed a significantly higher noise level (~ 2.5 orders of magnitude), it seems to be important that CCD and avalanche diodes are cooled further down, even for short integration times ($1 \mu s$). Especially in areas with critical radiation levels, EMCCD cameras should be considered as serious alternative to the

Transverse profile measurements and diagnostics systems

established MCP based ICCD systems. Second part of this investigation proofed the principle of a fiberoptic image bundle as a mechanically flexible alternative to telescope optics. Even though its signal performance was a factor of 40 lower than for the ICCD camera without the bundle, see Tab.2, we expect avoid most of the losses by direct coupling to the sensor. In this case the performance of the bundle should be limited just by its spectral transmission, which is still 35% for the relevant wavelength. With the BIF monitor embedded in an effective shielding, the image bundle opens up the field of application to radiative environments. We will set up a shielded BIF-monitor in a HEBT-line during the next beam time shortly. Dynamics of working gas ions have been simulated and identified as a considerable source of error for high intense or strongly focused ion beams, see Fig.12. To overcome this issue we currently are testing alternative working gases with shorter lifetimes.

ACKNOWLEDGEMENTS

We gratefully acknowledge T. Lehmann from the radiation and safety group for the discussion and his support with radioactive sources, H. Iwase and D. Schardt for their work and advice concerning numerical PHITS simulations. We wish to thank B. Lohmueller from Hamamatsu who provided the EMCCD camera for this measurements. This work was supported by the EU, project FP6-CARE-HIPPI.

REFERENCES

- [1] P. K. Roy et al., *Nuclear Instruments and Methods in Physics Research*, **A577**, p. 223 (2007)
- [2] GSI accelerators, further information on: www.gsi.de
- [3] FAIR Baseline Technical Report, Darmstadt, p. 1-38 (2006) www.gsi.de/fair/reports
- [4] R.H. Hughes et al., *Phys. Rev.* **123**, 2084 (1961), L.W. Dotchin et al., *J. Chem. Phys.* **59**, 3960 (1973)
- [5] Company Proxitronic, www.proxitronic.de
- [6] Company Basler, www.baslerweb.com
- [7] P. Forck, A. Bank, *Proc. EPAC 02*, Paris, p. 1885 (2002) and A. Bank, P. Forck, *Proc. DIPAC 03*, Mainz, p. 137 (2003)
- [8] see e.g. P. Forck et al., *Proc. DIPAC05*, p. 223, Lyon (2005)
- [9] F. Becker, C. Andre, P. Forck, *Proc. DIPAC07*, Venice (2007)
- [10] A. Ulrich et al., priv. communications, TU Munich (2008)
- [11] F. Becker, P. Forck, *Proc. EPAC06*, p. 1013, Edinburgh (2006) and F. Becker, A. Hug, P. Forck, P. Ni, D. Varentsov, *Las. and Part. Beams*, **24**, p. 541-551, Cambridge (2006)
- [12] H. Iwase et al., priv. communications, GSI, Darmstadt (2006) and H. Iwase et al., *JNST* **39 11**, 1142 (2002)
- [13] T. Kurosawa et al., *Phys. Rev. C* **62**, 044615 (2000)
- [14] F. Becker - *diploma thesis*, p. 34, Darmstadt (2006)
- [15] D. Schardt et al., priv. communications, Darmstadt (2008)
- [16] EMCCD detectors, general information, www.emccd.com
- [17] Comp. e2v, CCD097, back illuminated, www.e2v.com
- [18] free data basis: www.nndc.bnl.gov, www.nist.gov
- [19] Comp. Hamamatsu, (C-910013), www.hamamatsu.com
- [20] S. T. Park et al., *J. of Rad. and Nuc. Chem.*, Vol. **256**, No. **1**, p. 163-166, (2003)
- [21] N. Pyka, private communications, GSI, Darmstadt (2008)
- [22] P. Strehl, textbook: *Beam Instrumentation and Diagnostics*, Darmstadt, Germany Springer-Verlag, (2006)